

Impact of 3D Antenna Radiation Pattern in UAV Air-to-Ground Path Loss Modeling and RSRP-based Localization in Rural Area

Sung Joon Maeng, Hyeokjun Kwon, AND İsmail Güvenç, FELLOW, IEEE

¹Department of Electrical and Computer Engineering, North Carolina State University, Raleigh, NC 27606 USA

CORRESPONDING AUTHOR: Sung Joon Maeng (e-mail: smaeng@ncsu.edu).

This research is supported in part by the NSF award CNS-1939334. The data and the Matlab scripts for generating the results in this manuscript are available at [1].

ABSTRACT Ensuring reliable and seamless wireless connectivity for unmanned aerial vehicles (UAVs) has emerged as a critical requirement for a wide range of applications. The increasing deployment of UAVs has increased the significance of cellular-connected UAVs (C-UAVs) in enabling beyond-visual line of sight (BVLOS) communications. To ensure the successful operation of C-UAVs within existing terrestrial networks, it is vital to understand the distinctive characteristics associated with air-to-ground signal propagation. In this paper, we investigate the impact of 3D antenna patterns on a UAV air-to-ground path loss model, utilizing datasets obtained from a measurement campaign. We conducted UAV experiments in a rural area at various fixed heights, while also characterizing the 3D antenna radiation pattern by using an anechoic chamber facility. By analyzing reference signal received power (RSRP) using path loss models that account for antenna patterns, we observed that our measurement results, obtained at different UAV heights, aligned well with the two-ray path loss model when incorporating the measured antenna pattern. we propose an RSRP-based localization algorithm at a UAV that takes into account antenna patterns in both offline and online scenarios. Through our experimentation dataset, we show that incorporating measured antenna patterns significantly enhances the source localization accuracy.

INDEX TERMS 3D antenna pattern, AERPAW, air-to-ground, drone, ground reflection, localization, LTE, path loss, software-defined radio, UAV, USRP.

I. Introduction

Drones, also referred to as unmanned aerial vehicles (UAVs), have gained significant attention in recent years due to their wide range of promising applications. They are being increasingly utilized for various purposes in military, commercial, and public safety areas including surveillance [2], delivery services [3], drone taxi services [4], live video streaming, and search and rescue [5]. However, to fully realize the potential of these future applications, it is crucial to establish wireless connectivity with UAVs in beyond-visual-line-of-sight (BVLOS) scenarios. This can be achieved through the use of cellular-connected UAVs (C-UAVs), which enable seamless communication and data exchange between the UAVs and the ground base station (BS) [6].

To successfully operate C-UAVs using currently deployed terrestrial networks, it is crucial to have a comprehensive understanding of the unique characteristics associated with air-to-ground signal propagation. In particular, two key factors contribute to the radio propagation model: the elevation angle-dependent antenna radiation pattern and the strong ground reflection, which are not mainly considered in conventional terrestrial networks. In the ground-to-ground wireless connection, the altitude of the transmitter (Tx) and receiver (Rx) are often assumed fixed, and hence the corresponding radio propagation can often be reasonably modeled in the 2D space. However, as 3D geometry is considered in the air-to-ground C-UAV scenarios, the effects of the 3D antenna patterns and the ground reflection should be investigated more closely.

There have been several recent works in the literature focusing on UAV air-to-ground propagation models considering the impact of ground reflection and 3D antenna radiation patterns. In [7], the air-to-ground channel characteristic has been modeled using flight measurement datasets. The research demonstrated that the two-ray path loss model, which incorporates ground reflection, accurately matched the air-to-ground measurements. In [8], UAV air-to-ground channel has been measured in the open rural area employing various antenna orientation setups. The findings revealed a substantial impact of the elevation angle-dependent antenna pattern on the received signal power. In [9], the excess path loss in the cellular-to-UAV channel models due to the influence of antenna pattern has been explored. In [10], the impact of 3D antenna radiation patterns in a time difference of arrival (TDOA)-based 3D localization of UAVs has been studied, which reveals that the antenna pattern effect makes a significant difference in localization accuracy.

In this paper, we investigate the impact of the 3D antenna pattern and the ground reflection path in UAV air-to-ground path loss modeling. We conducted the experiments in the National Science Foundation (NSF) Aerial Experimentation and Research Platform on Advanced Wireless (AERPAW) testbed site [11]. We flew the UAV at various heights and collect long-term evolution (LTE) signals from the BS tower. Following the experiments, we post-process the collected LTE I/Q samples dataset and obtain the reference signal received power (RSRP) at different UAV locations. We analytically model air-to-ground radio propagation using different path loss models that incorporate the measured antenna patterns and the ground reflection. By comparing the received signal measurements with the path loss models derived analytically, we show that the 3D antenna pattern is a critical factor in the accurate air-to-ground channel model. Furthermore, through a comparison between the results obtained from the two-ray path loss model and the free space path loss model, we highlight the significance of including the ground reflection path in achieving an accurate air-to-ground path loss model. In addition, we propose a reference signal received power (RSRP)-based localization algorithm considering the impact of antenna patterns and apply the algorithm in localizing the source BS using the measurements collected from the AERPAW testbed. We evaluate the performance of both offline (at the end of the UAV flight) and online (real-time as the UAV flies) localization techniques. Simulation results show that accurate antenna pattern models can help significantly to improve localization accuracy.

This paper is organized as follows. In Section II, we describe the measurement campaign for the UAV experiment and LTE I/Q samples post-processing procedures. In Section III, we present air-to-ground propagation models by the path loss and the 3D antenna radiation pattern. In Section IV, we analyze the measured RSRP by the experiments by air-to-ground propagation models with different antenna

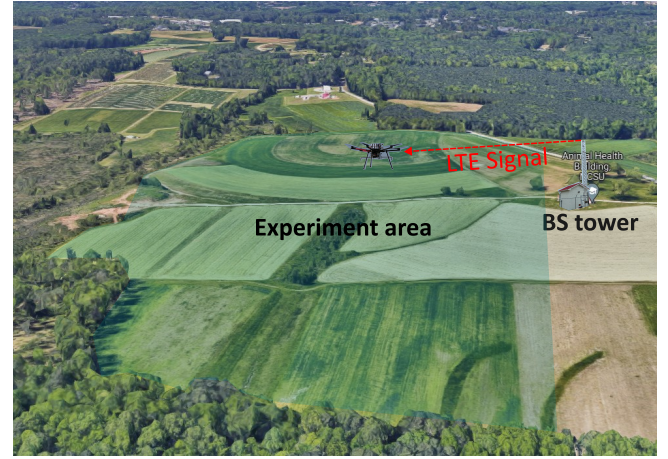


FIGURE 1. The AERPAW LWRFL site where UAV air-to-ground propagation data has been collected.

patterns. In Section V, we elaborate on the RSRP-based localization techniques for both offline and online scenarios. In Section VI, we evaluate the localization performance by using measured datasets by applying proposed algorithms, and the last section concludes the paper.

II. Measurement Campaign

In this section, we describe how we conduct the UAV and I/Q data collection experiments at NSF AERPAW Lake Wheeler Road Field Labs (LWRFL) site in Raleigh NC, USA.

A. UAV Experiment Setup

In our experiment, a BS tower transmits the LTE signal using the srsRAN open-source software-defined radio (SDR) software. We deploy a UAV that follows preprogrammed waypoints in a zig-zag pattern across the experiment site. During the flight, the UAV maintains a fixed height, and we repeat the experiments at different UAV heights, specifically 30 m, 50 m, 70 m, 90 m, and 110 m. To collect LTE I/Q samples from the BS tower and track the real-time location of the UAV, we equip the UAV with a portable node. The portable node consists of an SDR receiver and a GPS receiver. Regarding the configuration of the LTE evolved NodeB (eNB) at the BS tower, we set the tower height to 10 m, transmit power to 10 dBm, carrier frequency to 3.51 GHz, and bandwidth to 1.4 MHz. Both the BS tower and the UAV are equipped with USRP B205mini from National Instruments (NI). During the experiments, the UAV captures 20 ms segments of LTE signal out of every 100 ms. The snapshot of the experiment conducted at the AERPAW LWRFL is shown in Fig. 1.

B. LTE I/Q Samples Post-processing

After we finish the experiments, we post-process the collected LTE I/Q samples using MATLAB's LTE Toolbox. The cell search and synchronization procedures are carried out by detecting the primary synchronization signal (PSS) and the

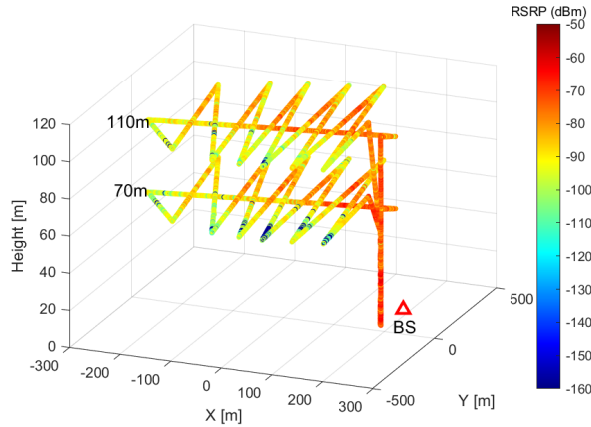


FIGURE 2. The trajectory of the UAV at two different altitudes. The RSRP is shown in different colors over the trajectory as indicated on the color bar. Collected LTE I/Q samples and GPS logs are post-processed to obtain the RSRP values.

secondary synchronization signal (SSS). Then, cell-specific reference signals (CRSs) are extracted by using physical cell identities (PCIs). In the end, RSRP is calculated by CRSs, which can be used as received signal strength. On top of the RSRPs of I/Q samples, we combine them with the GPS logs information, which gives the time and location information of the UAV. Fig. 2 shows the post-processing results of UAV trajectory along with the RSRPs from the measurement datasets. Note that other than having different altitudes, the UAV trajectories are otherwise identical. The color of the trajectory indicates the received signal strength (RSRP). It is clearly observed that the UAV flies up to a certain height and sweeps the experiment area by the zig-zag pattern while holding the height. After reaching the final waypoint, the UAV directly turns back to the landing point. Comprehensive discussion on how the data is post-processed and additional related results can be found in [12].

III. Air-to-ground Propagation Model

In this section, we consider path loss models and 3D antenna patterns to model and analyze the received signal strength. The received signal strength can be expressed as

$$r = P_{\text{Tx}} - PL + s, \quad (1)$$

where P_{Tx} , PL , and s denote the transmit power, the path loss, and the shadowing component, respectively.

A. Path Loss Model

To characterize the air-to-ground channel in the rural environment, we adopt the two-ray path loss model between a BS tower and a UAV. This model considers a line-of-sight (LoS) path as well as a strong ground reflection path, both contributing to the received signal. The path loss characterized by the two-ray ground reflection model can be

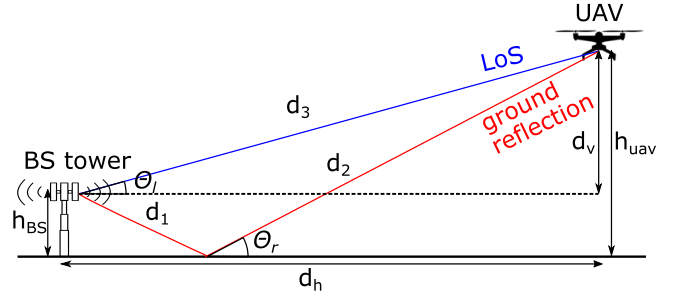


FIGURE 3. The illustration of the two-ray ground reflection model.

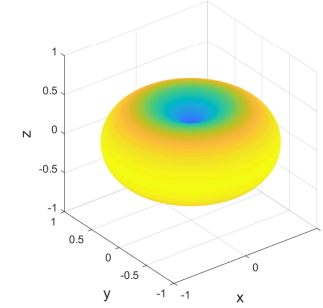


FIGURE 4. The 3D dipole antenna pattern of (5) used as the second antenna pattern option.

expressed as [13, Chapter 2]

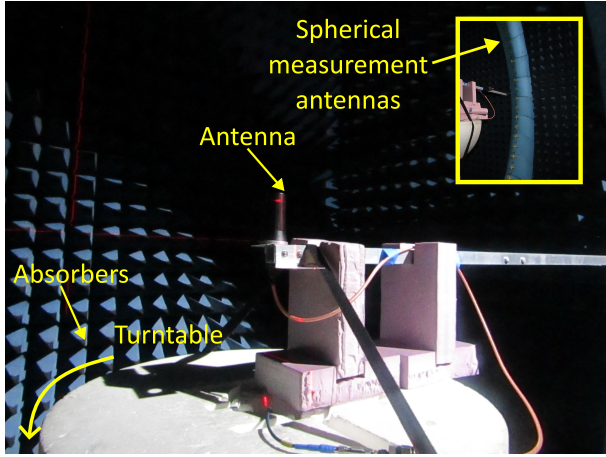
$$\begin{aligned} PL_{2R} = & \left(\frac{\lambda}{4\pi} \right)^2 \times \left| \frac{\sqrt{G_{\text{Tx}}(\phi_l, \theta_l)G_{\text{Rx}}(\phi_l, \theta_l)}}{d_3} \right. \\ & \left. + \frac{\Gamma(\theta_r) \sqrt{G_{\text{Tx}}(\phi_r, \theta_r)G_{\text{Rx}}(\phi_r, \theta_r)} e^{-j\Delta\tau}}{d_1 + d_2} \right|^2, \end{aligned} \quad (2)$$

where $G_{\text{Tx}}(\phi, \theta)$, $G_{\text{Rx}}(\phi, \theta)$ denote the antenna gain of a transmitter and a receiver from 3D antenna radiation patterns depending on azimuth (ϕ) and elevation (θ) angles, λ , $\theta_r = \tan^{-1} \left(\frac{h_{\text{BS}} + h_{\text{uav}}}{d_h} \right)$ indicate wave-length and the ground reflection angle, and $\Delta\tau = \frac{2\pi(d_1 + d_2 - d_3)}{\lambda}$ indicates the phase difference of two paths at the UAV. The distance and the angle parameters in the two-ray ground reflection model are described in Fig. 3. The ground reflection coefficient of the vertically polarized signal can be modeled as

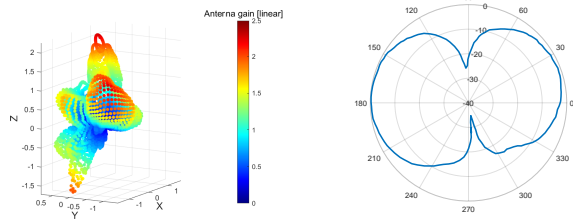
$$\Gamma(\theta_r) = \frac{\varepsilon_0 \sin \theta_r - \sqrt{\varepsilon_0 - \cos^2 \theta_r}}{\varepsilon_0 \sin \theta_r + \sqrt{\varepsilon_0 - \cos^2 \theta_r}}, \quad (3)$$

where ε_0 is the relative permittivity of the ground, which can be varied depending on the ground condition. If we only consider the LoS path in the two-ray path loss, we can obtain the free-space path loss model, given as

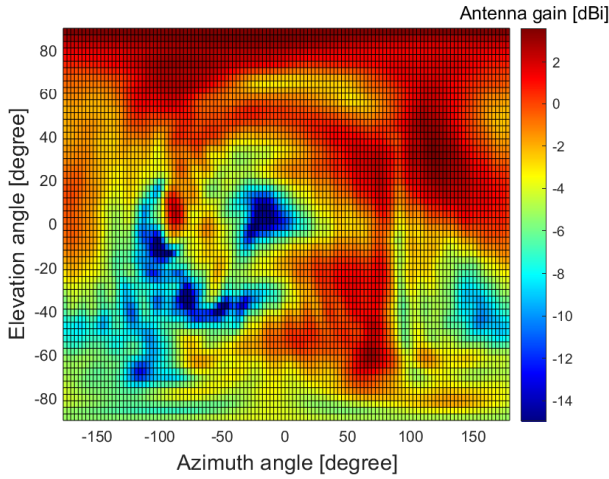
$$PL_{\text{FS}} = \left(\frac{\lambda}{4\pi} \right)^2 \left| \frac{\sqrt{G_{\text{Tx}}(\phi_l, \theta_l)G_{\text{Rx}}(\phi_l, \theta_l)}}{d_3} \right|^2. \quad (4)$$



(a) Anechoic chamber setup for Tx antenna pattern measurement. The center point of the chamber is adjusted to the tip of the antenna by the crossed laser lines.



(b) Measured Tx antenna pattern in Cartesian coordinates by the linear scale antenna gain. (c) Rx antenna pattern for the elevation angle domain by the dB scale in the specification sheet.



(d) Tx antenna pattern in 2D angles domain by dB scale antenna gain.

FIGURE 5. The photo of the anechoic chamber setup for the 3D antenna pattern measurement and the Tx, Rx antenna patterns we used for the analysis.

B. 3D Antenna Radiation Pattern

In this paper, we investigate the importance of accurate 3D antenna radiation patterns in UAV air-to-ground propagation models. While terrestrial networks typically rely on constant

antenna gain, which adequately captures the impact of omnidirectional antenna patterns in the azimuth angle domain, this approach may overlook the elevation angle-dependent antenna gain in the 3D topology of air-to-ground networks.

To observe the impact of different 3D antenna patterns, we consider three options: 1) a measured antenna pattern, 2) a dipole antenna pattern, and 3) a constant antenna pattern. In the first option of the measured antenna pattern, we utilize a measured 3D antenna pattern of Tx antenna (RM-WB1-DN) obtained from an anechoic chamber facility, available in IEEE DataPort [14], as well as an Rx antenna (SA-1400-5900) pattern from the specification sheet provided by the vendor [15]. For the second option, we adopt the elevation-angle dependent donut shape dipole antenna pattern expression for both Tx and Rx antennas, given as [16], [17]

$$G_{Tx}(\theta) = G_{Rx}(\theta) = \frac{\cos\left(\frac{\pi}{2}\cos\theta\right)}{\sin\theta}. \quad (5)$$

Fig. 4 shows the dipole antenna pattern obtained using the analytical dipole expression in (5). The pattern exhibits the characteristic donut shape associated with a typical dipole antenna.

Fig. 5a shows the setup for measuring the 3D antenna radiation pattern by using an anechoic chamber located at the Wireless Research Center (WRC), Wake Forest, NC. The Tx antenna is firmly installed at the center of the chamber, indicated by the intersection of laser lines. During the rotation of the turntable throughout a full circle, spherical measurement antennas capture the antenna gain across all elevation angles, enabling the generation of full 3D antenna patterns. The resulting pattern from the measurement is shown in Fig. 5b by the Cartesian coordinates, and Fig. 5d by using the azimuth and elevation angles coordinates, respectively. It is evident that the Tx antenna pattern is not the standard omnidirectional dipole antenna pattern but rather a complicated directional antenna pattern in the 3D domain. It implies that neither the constant antenna gain nor the doughnut shape dipole antenna pattern will accurately capture the antenna effects in air-to-ground signal propagation. Fig. 5c shows the antenna pattern in the elevation angle domain for the Rx antenna, as specified in the datasheet. It is observed that the Rx antenna pattern has the typical doughnut shape characteristic of a dipole pattern. Since this data for the Rx antenna was reasonably consistent with the measurements from our anechoic chamber, we decided to use the antenna pattern from the specification sheets for the Rx antenna.

IV. Analysis of Impact of 3D Antenna Patterns on Air-to-ground Radio Propagation

In this section, we conduct an evaluation to assess the impact of the three different 3D antenna patterns mentioned in Section B on 3D path loss modeling. In particular, we compare the RSRP values obtained by collected datasets with those derived from the analytical path loss models combined with 3D antenna patterns. To examine the diverse effects of the antenna radiation pattern, we present a comparison

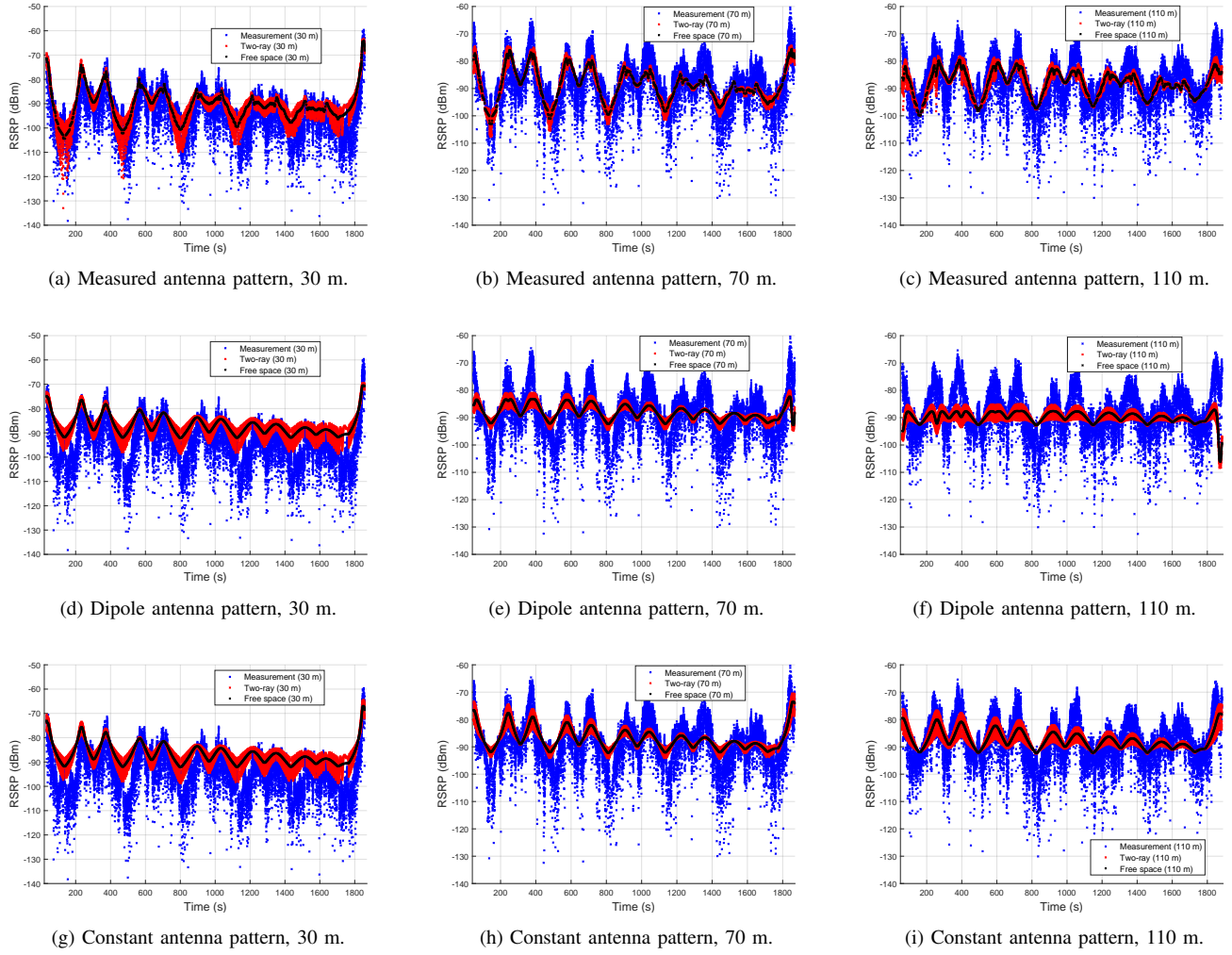


FIGURE 6. Compare measured RSRP with analytical path loss models using different antenna pattern setups in the time domain.

of the measured and analytically derived RSRPs in a single figure across different domains, including time, distance, and elevation angle. Note that due to space limitation concerns, we present selected results from three different UAV altitudes (30 m, 70 m, and 110 m) even though we collected the datasets at five different UAV altitudes.

A. Time, Distance, and Elevation Angle Domains Analysis

Fig. 6 shows the RSRP change in the time domain. We overlap the RSRP calculated by the analytical model on top of the RSRP obtained from the measurement, which shows how much the analytical results follow the measurement RSRP. In the analytical models, we individually consider three different antenna patterns. It is observed that the measured antenna pattern follows the fluctuation of the RSRP occurred by the zig-zag pattern of the trajectory for all three different heights in Fig. 6a, Fig. 6b, Fig. 6c, while the dipole and the constant antenna pattern do not fully capture the fluctuation of the RSRP, especially the deep fading and peak

in Fig. 6d, Fig. 6e, Fig. 6f, Fig. 6g, Fig. 6h, Fig. 6i. It implies that the constant or simple dipole antenna pattern models are not sufficient to characterize air-to-ground propagation. Moreover, it is critical to utilize the accurate antenna pattern in modeling the path loss. We also observe that the two-ray path loss model provides a more accurate representation of the deep fading phenomenon in RSRP compared with the free space path loss model. In addition, it is observed that the deep fading of RSRP is not captured by the constant antenna pattern while both deep fading and the peak of RSRP are not captured by the dipole antenna pattern in Fig. 6f, Fig. 6i. It implies that the antenna gain of a low elevation angle (deep fading) is overestimated in both the constant and the dipole antenna patterns while the antenna gain of a high elevation angle (peak) is underestimated in the dipole antenna pattern.

Fig. 7 shows the RSRP values according to the distance. As the results from the time domain, we observe that the measured antenna pattern presents the closest similarity with the RSRP from the measurement for all heights. In the dipole antenna pattern with 70 m UAV height, it is also observed

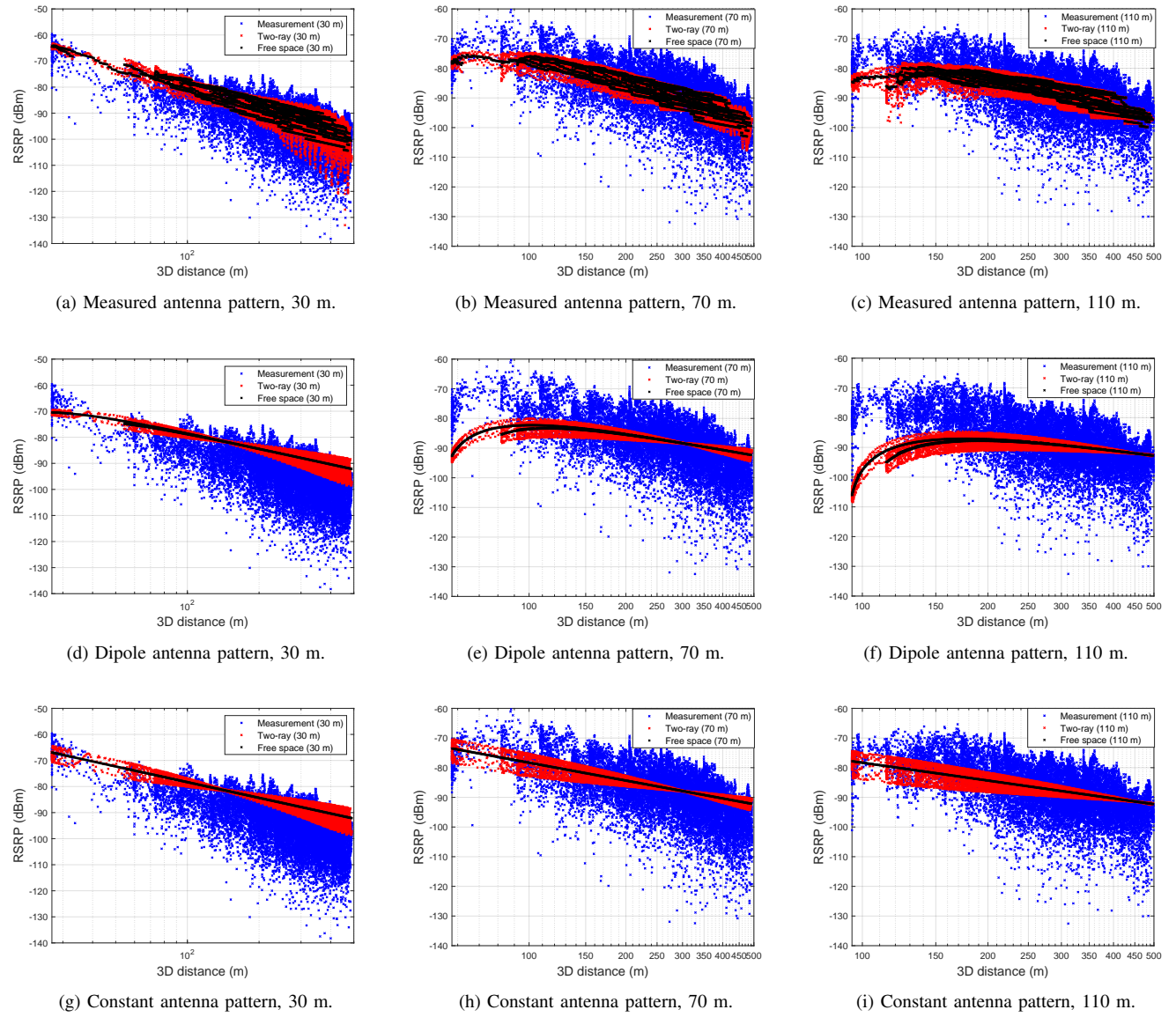


FIGURE 7. Compare measured RSRP with analytical path loss models using different antenna pattern setups in the distance domain.

that RSRP is underestimated/overestimated in the short/long distance. In the constant antenna pattern, the slope of the RSRP with the free space path loss model is constant since the path loss becomes only a function of distance in (4). However, the slope is not matched to the measurement RSRP as distance increases.

Finally, Fig. 8 shows the measurement and analytical RSRP depending on the elevation angle. In these results, we can clearly observe that the measured antenna pattern is the most accurate in the elevation domain when compared to the other two antenna patterns. In addition, the slope of the analytical RSRP in the dipole antenna pattern exhibits the poorest match with the corresponding measurement.

B. CDF Analysis

In Fig. 9, we show the cumulative distribution function (CDF) of RSRP for both measurement and analysis and the fitting error between RSRP of measurement and analysis. It is observed that the CDF of RSRP obtained from the measured antenna pattern is the closest to the RSRP of measurement for all heights. In addition, the two-ray path loss model achieves a similar CDF curve to the free-space model compared with RSRP plots in Fig. 6, Fig. 7, Fig. 8 where the accuracy between the two-ray and the free space path loss model is clearly observed. The fitting error in Fig. 9d, Fig. 9e, Fig. 9f is calculated by the absolute difference between measurement RSRP and analytical RSRP. We observe that the fitting error is the smallest by the measured antenna pattern for all heights, especially the gap

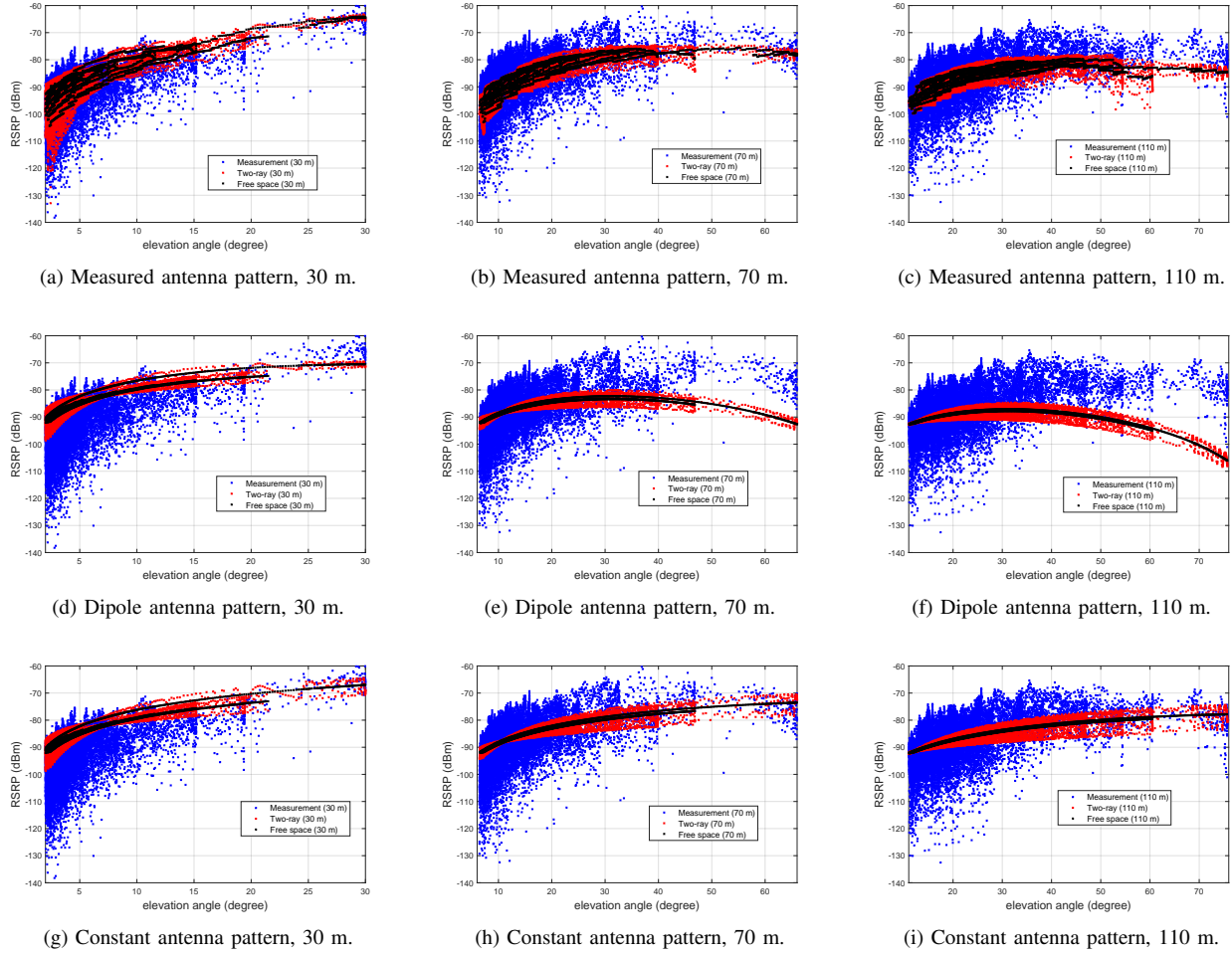


FIGURE 8. Compare measured RSRP with analytical path loss models using different antenna pattern setups in the elevation domain.

between the measured antenna pattern and other antenna patterns is the largest at 30 m height.

C. Antenna Pattern Estimation

In previous antenna pattern analysis results, we plug 3D antenna patterns in the path loss models and compare the measured RSRP with the analytical RSRP. In this subsection, we take a reverse approach: we estimate the 3D antenna pattern from the RSRP measurements and compare the estimated antenna pattern with the measured antenna pattern from the anechoic chamber (see Fig. 5). Fig 10a shows the combined total antenna pattern of the Tx and Rx with respect to the elevation and azimuth angles. To obtain the combined antenna pattern, we utilize the Tx antenna pattern shown in Fig. 5d and the Rx antenna pattern shown in Fig. 5c. In Fig. 10b, we present the estimated 3D antenna pattern in the azimuth and the elevation angles domain. To estimate the antenna pattern, we utilize all available UAV height datasets, including 30 m, 50 m, 70 m, 90 m, and 110 m. Since we have access to the 3D location of the UAV for each RSRP measurement through GPS logs, we can determine

the azimuth and elevation angles of the LoS between the BS tower and the UAV. By subtracting transmit power and the free space path loss component without antenna patterns from RSRP value, we can obtain the estimated 3D antenna pattern, which is given by

$$\hat{G}_{\text{tot}}(\phi_x, \theta_y) = \frac{1}{N_{xy}} \sum_{i=1}^{N_{xy}} [\text{RSRP}^i(\phi_x, \theta_y) - P_{\text{Tx}} + \text{PL}_{\text{FS}}^i(\phi_x, \theta_y)], \quad (6)$$

where N_{xy} denote the number of RSRP samples where the UAV are located at ϕ_x azimuth angle of LoS and θ_y elevation angle of LoS, and PL_{FS}^i indicates free space path loss in (4) with $G_{\text{Tx}}(\phi_x, \theta_y) = G_{\text{Rx}}(\phi_x, \theta_y) = 1$.

Note that the estimated antenna pattern may have limitations in terms of accuracy, particularly when it comes to removing the effects of shadowing and ground-reflected signals. These limitations become more apparent when the number of samples from the measurements is insufficient. From Fig. 10b. it is observed that the estimated antenna pattern occupies a restricted angle space that aligns with the trajectory of the flight. It spans approximately from 5 to 160

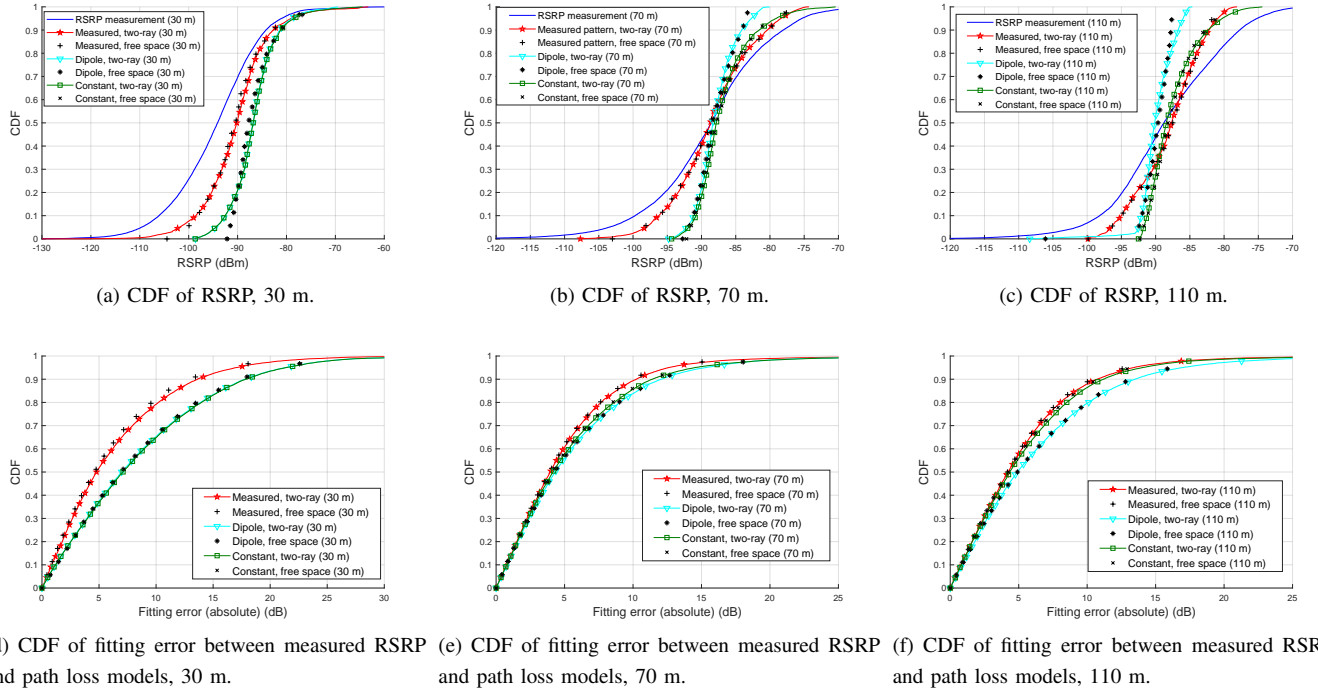


FIGURE 9. CDF of RSRP and the fitting error to observe the similarity between measured RSRP and analytical RSRP. All the three different antenna pattern options are considered.

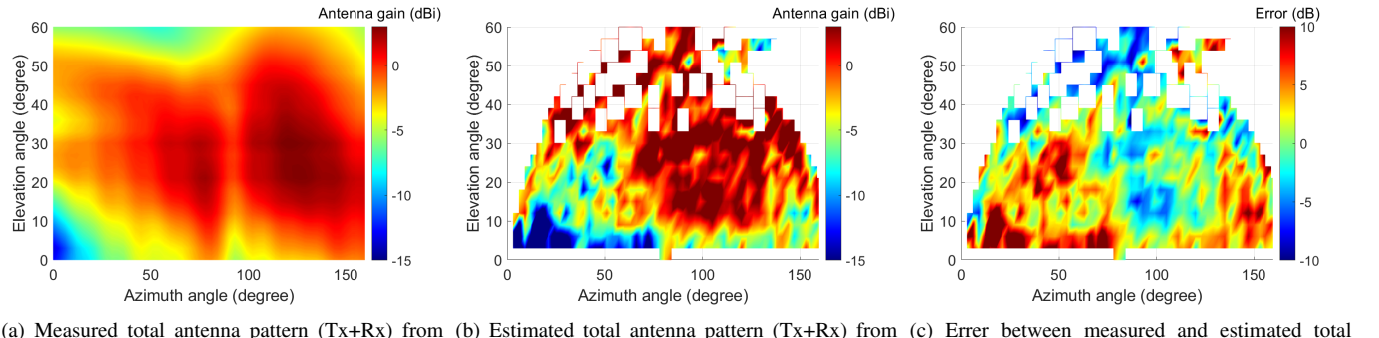


FIGURE 10. Comparison of (a) measured antenna pattern with (b) the estimated antenna pattern. (c) The error of the antenna pattern is generated by subtracting (b) the estimated antenna pattern from (a) the measured antenna pattern.

degrees in the azimuth angle range and from 5 to 60 degrees in the elevation angle range. The white spaces in the figure occur because they correspond to angles that fall outside the range of the UAV's flying area. In such cases, we can easily interpolate the unknown antenna patterns to estimate their characteristics, which will be studied in future work. Comparing with the measured antenna pattern in Fig. 10a, we observe an overall similarity in terms of directivity. High antenna gain is observed in the azimuth angle range of 60 to 140 degrees and the elevation angle range of 10 to 40 degrees. However, the accuracy of the estimated antenna pattern degrades in certain angle ranges due to the limited number of samples available in the measurement datasets.

Fig. 10c shows the relative error between the measured antenna pattern in Fig. 10a and the estimated antenna pattern in Fig. 10b. We observe that the mismatch between the two antenna patterns is relatively low within certain angle ranges. Specifically, the azimuth angle range of 60 to 140 degrees and the elevation angle range of 10 to 40 degrees exhibit a low level of mismatch. On the other hand, the mismatch between the antenna patterns is high within some other angle ranges. In particular, the azimuth angle range of 10 to 80 degrees and the elevation angle range of 5 to 10 degrees exhibit a higher level of mismatch.

V. Localization of BSs by Using UAVs

In this section, we focus on the problem of localizing the source BS by using the collected RSRP data over the trajectory of the UAV. In particular, we propose the air-to-ground propagation-based localization algorithm considering 3D antenna patterns. Note that while localization of a ground BS may have its own use cases and merits, the proposed solution is generic and can also be applied in other scenarios where a UAV aims to localize a different ground signal source.

A. RSRP-based Least Square Estimation

The 3D location of a BS and a UAV can be represented by

$$\mathbf{l}^{\text{bs}} = (\omega^{\text{bs}}, \psi^{\text{bs}}, h^{\text{bs}}), \mathbf{l}_i^{\text{uav}} = (\omega_i^{\text{uav}}, \psi_i^{\text{uav}}, h_i^{\text{uav}}), \quad (7)$$

where ω , ψ , and h denote the longitude, latitude, and altitude of the BS location, which can be obtained by the GPS sensors of the UAV. The discrete-time location of the UAV during the flight is indicated by $\mathbf{l}_i^{\text{uav}}$. The horizontal distance between a BS and a UAV can be expressed as

$$\begin{aligned} d_{\text{h},i} &= \arccos \left(\sin \psi_i^{\text{uav}} \sin \psi^{\text{bs}} + \cos \psi_i^{\text{uav}} \right. \\ &\quad \left. \cos \psi^{\text{bs}} \cos(\omega^{\text{bs}} - \omega_i^{\text{uav}}) \right) R, \\ &\approx \sqrt{(\omega^{\text{bs}} - \omega_i^{\text{uav}})^2 \cos(\psi_0)^2 + (\psi^{\text{bs}} - \psi_i^{\text{uav}})^2} \frac{R\pi}{180}, \end{aligned} \quad (8)$$

where $R \approx 6378137$ m denotes the radius of earth. The approximation in (8) comes from the equirectangular projection, transforming spherical coordinates into planar coordinates [18], and ψ_0 denotes the standard parallels decided by the scale of the projection. Note that since the size of the area of the experiment site is small, the approximation is sufficiently accurate. The vertical distance between a BS and a UAV is given by $d_v = |h^{\text{bs}} - h_i^{\text{uav}}|$. Then, the 3D distance (d_3) between a BS and a UAV can be calculated by

$$d_{3,i}^2 = d_{\text{h},i}^2 + d_v^2. \quad (9)$$

From (1) and (4), the received signal strength (RSRP) can be reformulated as

$$r_i = \frac{P_{\text{Tx}} \lambda^2}{(4\pi)^2} \frac{G_{\text{Tx},i} G_{\text{Rx},i}}{d_{3,i}^2} + \tilde{s}, \quad (10)$$

where \tilde{s} indicates additive components including shadowing and ground reflected signal. Then, by neglecting the additive components \tilde{s} , we can represent the distance as follow:

$$d_{3,i}^2 = \frac{P_{\text{Tx}} \lambda^2}{(4\pi)^2} \frac{G_{\text{Tx},i} G_{\text{Rx},i}}{r_i}. \quad (11)$$

To formulate the least square (LS) estimator using multiple RSRP measurements over the trajectory of the UAV, we first subtract the square of the 3D distance at a reference UAV location (r) from all other UAV locations (i) [19], [20], which can be written as follows:

$$\begin{aligned} d_{3,r}^2 - d_{3,i}^2 &= \left(\frac{R\pi}{180} \right)^2 \left\{ (\omega^{\text{bs}} - \omega_r^{\text{uav}})^2 \cos(\psi_0)^2 + \right. \\ &\quad \left. (\psi^{\text{bs}} - \psi_r^{\text{uav}})^2 - (\omega^{\text{bs}} - \omega_i^{\text{uav}})^2 \cos(\psi_0)^2 - (\psi^{\text{bs}} - \psi_i^{\text{uav}})^2 \right\}, \end{aligned} \quad (12)$$

Algorithm 1 Fixed-point Iterative Algorithm for Localization

```

1: Input:  $r_i, \omega_i^{\text{uav}}, \psi_i^{\text{uav}} \forall i, P_{\text{Tx}}, G_{\text{Tx}}^{\text{pat}}(\omega, \phi), G_{\text{Rx}}^{\text{pat}}(\omega, \phi)$ 
2: Initialize:  $G_{\text{Tx},i}^{(1)} = 1, G_{\text{Rx},i}^{(1)} = 1 \forall i$ 
3: Iterations:
4: for  $k = 1, \dots, K$  do
5:   Calculate  $\mathbf{A}^{(k)}, \mathbf{B}^{(k)}$  by (15)
6:   Obtain  $\hat{\mathbf{l}}^{(k)}$  by solving LS estimator in (13)
7:   Update  $G_{\text{Tx},i}^{(k+1)}, G_{\text{Rx},i}^{(k+1)} \forall i$  from the estimated location of the BS  $\hat{\mathbf{l}}^{(k)}$ , and antenna patterns  $G_{\text{Tx}}^{\text{pat}}(\omega, \phi), G_{\text{Rx}}^{\text{pat}}(\omega, \phi)$ 
8: end for

```

where $d_{3,r}, \psi_r^{\text{uav}}, \omega_r^{\text{uav}}$ denote the 3D distance and the coordinates of the reference point, respectively, and $i = 1, \dots, N$ where N is the number of UAV locations where the RSRPs will be used for localization, excluding the reference location r . By reorganizing (12) in matrix form for $i = 1, \dots, N$, we can obtain the following linear expression:

$$\mathbf{A} \hat{\mathbf{l}} = \mathbf{B}, \quad (13)$$

where $\mathbf{A}, \mathbf{B}, \hat{\mathbf{l}}$ are given at the top of next page in (15). After simplifying (12) and substituting $d_{3,r}^2$ and $d_{3,i}^2$ into (11), we can obtain \mathbf{A}, \mathbf{B} . Finally, we can obtain the estimated location of the BS (longitude and latitude) $\hat{\mathbf{l}}$ by multiplying both sides of (13) with the Moore-Penrose inverse of \mathbf{A} (\mathbf{A}^\dagger), which is given by

$$\hat{\mathbf{l}} = \mathbf{A}^\dagger \mathbf{B}, \quad (14)$$

Note that the localization accuracy depends critically on the RSRPs used at specific locations over the trajectory of the UAV, i.e., the set of $\mathbf{l}_i^{\text{uav}}$ for $i = 1, \dots, N$. In this work, we consider both random and more structured approaches of selecting $\mathbf{l}_i^{\text{uav}}$ over the UAV's trajectory, and compare their localization performance.

B. Fixed-point Iterative Algorithm

The LS estimator solution for the localization problem in (14) requires the antenna gains $G_{\text{Tx}}, G_{\text{Rx}}$ for constructing \mathbf{B} . However, the antenna gains are also the function of the location of the BS $\omega^{\text{bs}}, \psi^{\text{bs}}$, which is what we are aiming to estimate. Therefore, we propose a fixed-point iterative algorithm to solve for the BS's location, where: 1) the LS estimator is solved by given antenna gains; 2) the antenna gain is updated by the estimated BS location; and finally, 3) the estimated BS location is re-updated by the LS estimator with the updated antenna gain. We initialize the antenna gain as 1 for all UAV locations (constant antenna pattern) and we utilize the given antenna patterns (measured, dipole, constant) from the second iteration. In this way, we take into account the impact of the antenna pattern to improve the localization performance. The detailed steps are described in Algorithm 1. We denote antenna patterns as $G_{\text{Tx}}^{\text{pat}}(\omega, \phi), G_{\text{Rx}}^{\text{pat}}(\omega, \phi)$.

$$\begin{aligned}
\mathbf{A} &= \begin{bmatrix} (-2\omega_r^{\text{uav}} + 2\omega_1^{\text{uav}}) \cos(\psi_0)^2 & \cdots & (-2\omega_r^{\text{uav}} + 2\omega_N^{\text{uav}}) \cos(\psi_0)^2 \\ -2\psi_r^{\text{uav}} + 2\psi_1^{\text{uav}} & \cdots & -2\psi_r^{\text{uav}} + 2\psi_N^{\text{uav}} \end{bmatrix}^T \\
\mathbf{B} &= \begin{bmatrix} \left(\frac{180}{R\pi}\right)^2 \frac{P_{\text{Tx}}\lambda^2}{(4\pi)^2} \left(\frac{G_{\text{bs},r}G_{\text{uav},r}}{r_r} - \frac{G_{\text{bs},1}G_{\text{uav},1}}{r_1}\right) - (\omega_r^{\text{uav}})^2 + (\omega_1^{\text{uav}})^2 + (-(\omega_r^{\text{uav}})^2 + (\omega_1^{\text{uav}})^2) \cos(\psi_0)^2 \\ \vdots \\ \left(\frac{180}{R\pi}\right)^2 \frac{P_{\text{Tx}}\lambda^2}{(4\pi)^2} \left(\frac{G_{\text{Tx},r}G_{\text{Rx},r}}{r_r} - \frac{G_{\text{Tx},N}G_{\text{Rx},N}}{r_N}\right) - (\omega_r^{\text{uav}})^2 + (\omega_N^{\text{uav}})^2 + (-(\omega_r^{\text{uav}})^2 + (\omega_N^{\text{uav}})^2) \cos(\psi_0)^2 \end{bmatrix} \\
\hat{\mathbf{I}} &= [\hat{\omega}^{\text{bs}} \quad \hat{\psi}^{\text{bs}}]^T.
\end{aligned} \tag{15}$$

C. Offline Localization

In this section, we describe the offline localization method using the Algorithm 1. In the offline mode, we utilize the entire dataset after finishing the UAV flight to localize the BS tower location. For instance, the input dataset of Algorithm 1 r_i , ω_i^{uav} , ψ_i^{uav} can be randomly chosen N samples out of the whole dataset where $i = 1, \dots, N$ to estimate the location of the BS tower $\hat{\mathbf{I}}^{\text{bs}}$. The antenna patterns $G_{\text{Tx}}^{\text{pat}}(\omega, \phi)$, $G_{\text{Rx}}^{\text{pat}}(\omega, \phi)$ can be considered by the measured, dipole, and constant antenna patterns.

D. Online Localization

In this section, we propose a real-time algorithm for online localization by adopting the RSRP-based fixed-point iterative algorithm in Algorithm 1. As a UAV collects the received signal and obtains RSRP from the new measurement, it continuously updates the estimated location of the signal source in real-time. This updating process leverages the estimated locations obtained from previous measurements, along with the new measurement, to refine the localization estimate. In the proposed online localization algorithm, we randomly pick M RSRP samples out of the N_{buf} samples in the buffer of collected RSRP, which can be given by $\mathbf{r}_{\text{buf}} = \{r_1, \dots, r_{N_{\text{buf}}}\}$ where the maximum size of buffer is N_{max} . Besides, the coordinates of the UAV with the corresponding RSRPs are buffered in $\omega_{\text{buf}} = \{\omega_1, \dots, \omega_{N_{\text{buf}}}\}$, $\psi_{\text{buf}} = \{\psi_1, \dots, \psi_{N_{\text{buf}}}\}$. If the size of the buffer becomes full, the new RSRP replaces the most outdated RSRP. After that, we apply Algorithm 1 and obtain the estimated location $\hat{\mathbf{I}}$. Note that in the offline localization, N samples are chosen from the entire dataset once, while in the online localization, M samples are selected from the buffer for every data collection, and J times data collections are executed.

We further consider a weighted localization algorithm where multiple location estimates are combined after being scaled with their normalized confidence weights. The motivation is that due to the non-uniform antenna patterns in 3D, the use of certain combinations of UAV locations for estimating the source location will be more favorable than other locations. Such weighted localization approaches have been used extensively in the literature for non-line-of-sight mitigation, see e.g. [21] and the references therein. The confidence of each estimated location can be characterized based on the residual for that location estimate [22], which

can be expressed as

$$e_{\text{res},j} = \frac{1}{M} \sum_{i=1}^M |d_{3,i} - \hat{d}_{3,i}(\hat{\omega}^{\text{bs}}, \hat{\psi}^{\text{bs}})|^2, \tag{16}$$

where $d_{3,i}$ comes from (11) and $\hat{d}_{3,i}(\hat{\omega}^{\text{bs}}, \hat{\psi}^{\text{bs}})$ is calculated by (8), (9). Then, the weight of the estimated location can be written as follows:

$$\mu_j = \frac{N_{\text{buf}}}{\log_{10}(e_{\text{res},j})}. \tag{17}$$

As the residual is smaller and the size of the buffer is larger, the weight of the estimated location is higher. The real-time estimated location of the signal source can be updated by the weighted linear combination, which is given by

$$\hat{\mathbf{I}}^* = \frac{\sum_{k=1}^j \hat{\mathbf{I}}_k \mu_k}{\sum_{k=1}^j \mu_k}. \tag{18}$$

The detailed algorithm of the online localization is described in Algorithm 2. In the algorithm, $\mathbf{x}_{\setminus x_1}$ represents the operation that excludes x_1 entry from \mathbf{x} .

Instead of choosing M samples randomly from the buffers in line 13 of Algorithm 2, we can also explore alternative strategies for sample selection. The first option can be the equal interval selection, which chooses samples with equal intervals from the buffer. Since measurements are periodically conducted with uniform time intervals, the selected samples have equal time intervals. Therefore, the index of M samples from the equal interval selection can be $1, \lfloor \frac{N_{\text{buf}}}{M} \rfloor, \lfloor \frac{2N_{\text{buf}}}{M} \rfloor, \dots, N_{\text{buf}}$ where $\lfloor x \rfloor$ denotes the round operation.

The second option for sample selection is the nearby waypoints selection strategy. This approach involves utilizing samples that are in close proximity to the waypoints along the UAV's route. The waypoints serve as reference points that outline the trajectory of the UAV, allowing us to choose a set of samples that are spatially well separated. If the number of waypoints contained in the buffer is smaller than M , we choose multiple samples that are nearby the same waypoint to fulfill the M sample requirement. For example, if the buffer contains samples around waypoints 1, 2, 3, and 4, and we need $M = 10$ samples. In this case, we pick 3 samples from each of waypoints 1 and 2, and 2 samples from each of waypoints 3 and 4.

Algorithm 2 Online Localization

```

1: for  $j = 1, \dots, J$  do
2:   New dataset:
3:   Collect  $r^{(j)}, \omega^{\text{uav}(j)}, \psi^{\text{uav}(j)}$  from the new measurement
4:   Buffers update:
5:   if  $N_{\text{buf}} < N_{\text{max}}$  then
6:      $\mathbf{r}_{\text{buf}} \leftarrow [\mathbf{r}_{\text{buf}}, r^{(j)}]$ ,  $\omega_{\text{buf}}^{\text{uav}} \leftarrow [\omega_{\text{buf}}, \omega^{\text{uav}(j)}]$ ,
7:      $\psi_{\text{buf}}^{\text{uav}} \leftarrow [\psi_{\text{buf}}, \psi^{\text{uav}(j)}]$ 
8:   else if  $N_{\text{buf}} \geq N_{\text{max}}$  then
9:      $\mathbf{r}_{\text{buf}} \leftarrow [\mathbf{r}_{\text{buf}} \setminus \mathbf{r}_1, r^{(j)}]$ ,
10:     $\omega_{\text{buf}}^{\text{uav}} \leftarrow [\omega_{\text{buf}}^{\text{uav}} \setminus \omega_1, \omega^{\text{uav}(j)}]$ ,  $\psi_{\text{buf}}^{\text{uav}} \leftarrow [\psi_{\text{buf}}^{\text{uav}} \setminus \psi_1, \psi^{\text{uav}(j)}]$ 
11:   end if
12:   Localization:
13:   Randomly choose  $M$  samples from  $\mathbf{r}_{\text{buf}}, \omega_{\text{buf}}^{\text{uav}}, \psi_{\text{buf}}^{\text{uav}}$ 
14:   And, obtain a estimated location  $\hat{\mathbf{l}}^{(j)}$  from  $M$  samples by applying Algorithm 1
15:   Weighted linear combination:
16:   Calculate the weight  $\mu^{(j)}$  from (16), (17)
17:   Update a real-time estimated location by  $\hat{\mathbf{l}}^{*(j)} = \frac{\sum_{k=1}^j \hat{\mathbf{l}}^{(k)} \mu^{(k)}}{\sum_{k=1}^j \mu^{(k)}}$ 
18: end for

```

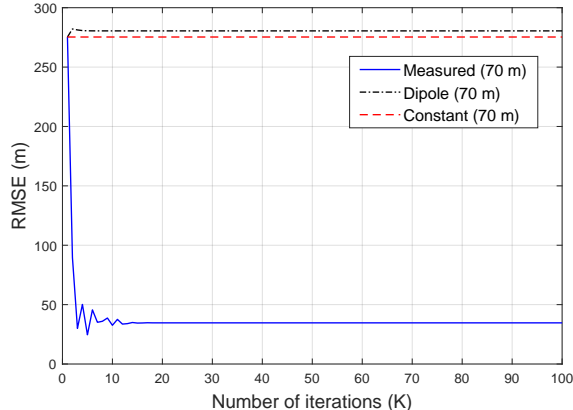


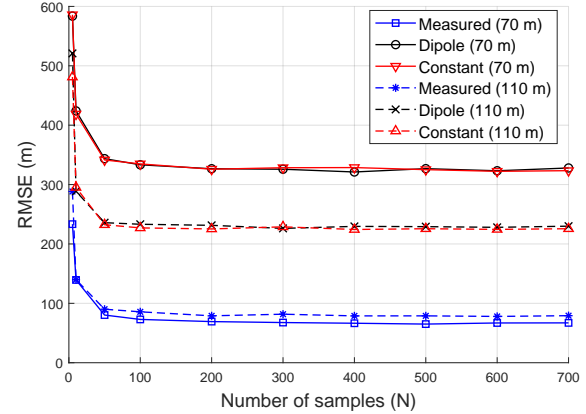
FIGURE 11. The convergence of Algorithm 1 with different antenna patterns where the number of samples $N = 300$.

VI. Numerical Results

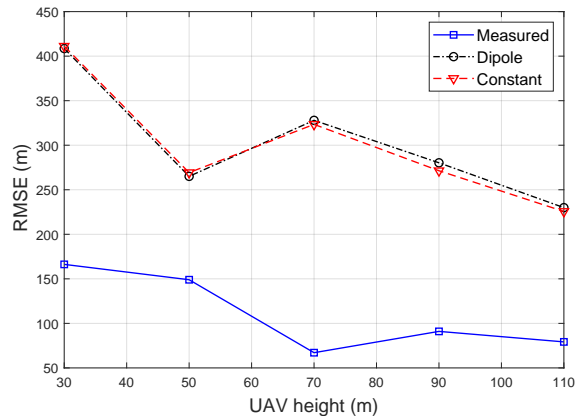
In this section, we evaluate the performance of the localization with different antenna patterns discussed in Section V, considering both the offline and the online approaches. In the offline mode, the BS tower is localized using the entire dataset, while real-time localization is examined in the online mode.

A. Performance of Offline RSRP-based Localization

First, in this subsection, the location of the BS tower is estimated by RSRP obtained from offline datasets collected by the UAV. To enhance the accuracy, we initially apply a moving average filter across all RSRP samples to mitigate the impact of rapid fluctuations. Subsequently,



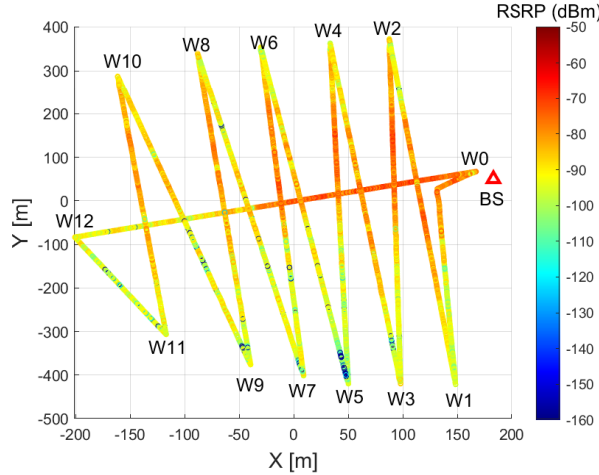
(a) Convergence of RMSE at 70 m and 110 m UAV heights.



(b) Converged RMSE vs. UAV height.

FIGURE 12. (a) The RMSE as the number of samples (UAV locations where RSRPs are used) increases to localize the BS in the offline mode ($K = 50$ in Algorithm 1). (b) Localization RMSE after convergence versus the UAV height.

we employ Algorithm 1 for the localization process. We consider the three types of antenna patterns discussed earlier in Section B (measured, dipole, constant). Fig. 11 shows the convergence of the iterative algorithm. The root mean square error (RMSE) is calculated based on the distance error $\sqrt{(\omega^{\text{bs}} - \hat{\omega}^{\text{bs}})^2 \cos(\psi_0)^2 + (\psi^{\text{bs}} - \hat{\psi}^{\text{bs}})^2 \frac{R\pi}{180}}$ from (8). It is observed that when considering the measured antenna pattern, the distance error is significantly reduced as the number of iterations increases, converging in less than 20 iterations. However, the dipole antenna pattern does not improve the distance error. This is due to the fact that the measured antenna pattern accurately captures RSRP and reduces the distance error through iterative updates of the estimated locations. In contrast, the dipole antenna pattern does not improve localization performance as it lacks precision compared to the constant antenna pattern. It is worth noting again that we initialize all the algorithms with the constant antenna gain at the first step of the iterations.



(a) Waypoints and route of the UAV for the online localization.

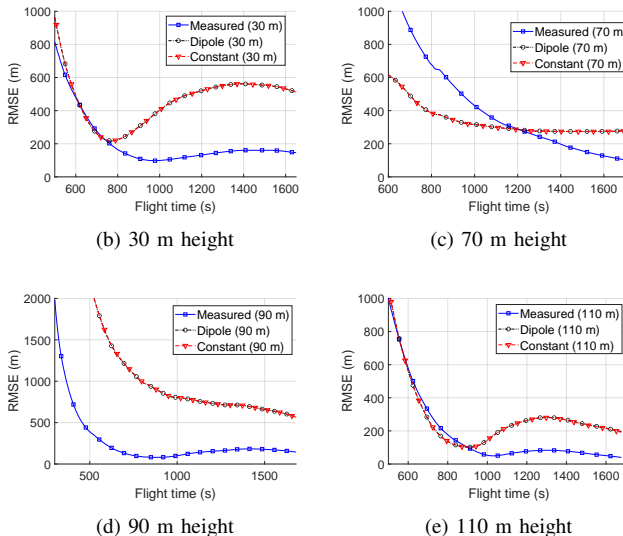


FIGURE 13. (a) The route of the UAV for online localization, where we consider that UAV follows the path $W_{11} - W_{10} - \dots - W_0$. (b)-(e) The RMSE as a function of flight time in the online localization method using Algorithm 2 with different UAV heights.

In our offline localization, we evaluate the RMSE as the number of samples increases for different UAV heights. We randomly choose N samples from the offline collected datasets. In Fig. 12, we observed that adopting the measured antenna pattern resulted in higher localization accuracy compared to considering the dipole antenna pattern and constant antenna pattern. This indicates that accurate antenna pattern modeling is critical in improving localization performance.

B. Performance of Online RSRP-based Localization

In this section, we evaluate the performance of BS localization in a real-time scenario using the online mode. During data collection by the UAV, localization is carried out in real-time. Fig. 13a shows the trajectory and waypoints followed by the UAV during the measurement. In the original data collection experiment, the UAV flies away from the BS

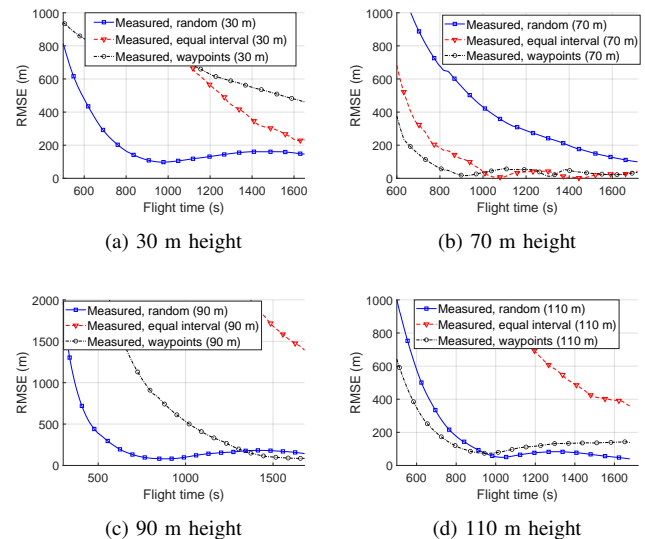


FIGURE 14. Localization RMSE versus flight time with three different RSRP selection strategies over the trajectory of the UAV, in line 13 of Algorithm 2, for localizing the signal source.

starting from W_0 and proceeding to W_{12} , before returning back to W_0 following the path $W_0 - W_1 - \dots - W_{12} - W_0$. On the other hand, the UAV flying toward the BS is a more relevant scenario for online localization. Therefore, we consider the route $W_{11} - W_{10} - \dots - W_0$ and the corresponding RSRP measurements over this trajectory for testing the online localization techniques. Considering this route, Fig. 13b, Fig. 13c, Fig. 13d, and Fig. 13e show the RMSE as a function of the UAV flight time for different heights. We employ Algorithm 2 for the online localization of the BS, using $M = 10$ RSRP measurements from the past locations over the UAV's trajectory, with $N_{\max} = 10000$. It is observed that in all heights, the RMSE decreases as the flight time increases, and the measured antenna pattern achieves a smaller RMSE compared to the dipole and constant antenna patterns at the end of flight time. However, we also observe that early on during the UAV's flight, the dipole and the constant antenna patterns outperform the measured antenna pattern at 30 m, 70 m, and 110 m UAV altitudes. This observation holds true until around 750 s for the 30 m UAV height, 1200 s for the 70 m UAV height, and 900 s for the 110 m UAV height.

Fig. 14 compares the RMSE of online localization using other alternative approaches to the random selection of the UAV locations where the RSRPs will be used for localization. In particular, on line 13 of Algorithm 2, we have the option to randomly select M samples from the buffers. However, instead of random selection, we also consider two alternative strategies: equal interval selection and nearby waypoints selection, which were discussed in Section D. These strategies introduce temporal and spatial separation among the selected samples, respectively. The results show that the random selection strategy outperforms others at 30 m

and 110 m heights, while the nearby waypoints selection strategy achieves the best performance at 70 m and 90 m heights. In addition, the equal interval selection and the nearby waypoints selection strategies perform poorly at 90 m and 110 m heights, and 70 m height, respectively. It implies that the random selection strategy generally yields good performance across all height datasets. On the other hand, while the equal interval selection and nearby waypoints selection strategies can outperform the random selection strategy in certain cases, they may also result in poor performance depending on the specific heights being considered.

VII. Conclusion

In this paper, we study the impact of 3D antenna radiation patterns in air-to-ground path loss modeling. We collect I/Q samples in C-band using an SDR receiver carried by a UAV in a rural environment, to capture signals from an SDR-based LTE BS. The obtained I/Q samples are then post-processed to obtain the RSRP from the target LTE transmission. We model the 3D antenna radiation pattern by using antenna measurements in an anechoic chamber. Then, we can compare the measurement RSRP with the analytical RSRP, obtained using the proposed path loss models that take into account the 3D antenna patterns. We also evaluate the accuracy of analytical RSRP considering dipole and constant-gain antenna patterns, where we observe significantly better path loss modeling accuracy when the measured antenna patterns are used. Moreover, we propose an RSRP-based fixed-point iterative localization solution in both offline and real-time online localization scenarios, and we show that the localization accuracy is improved significantly when accurate 3D antenna patterns are used as side information. Finally, we estimate the 3D antenna pattern using the measurement RSRP and compare it with the antenna pattern measured at the anechoic chamber. We observe that the directivity of the antenna pattern is similar between the measured and estimated antenna patterns.

REFERENCES

- [1] S. J. Maeng, O. Ozdemir, I. Guvenc, M. Sichitiu, and R. Dutta, “LTE I/Q Measurement by AERPAW Platform for Air-to-Ground Propagation Modeling,” *IEEE Dataport*, 2022. [Online]. Available: <https://dx.doi.org/10.21227/0p43-0d72>
- [2] K. Namuduri, U.-C. Fiebig, D. Matolak, I. Guvenc, K. Hari, and H.-L. Maattanen, “Advanced Air Mobility: Research Directions for Communications, Navigation, and Surveillance,” *IEEE Veh. Technol. Mag.*, pp. 2–10, Dec. 2022.
- [3] Insider Intelligence. (2023) Why Amazon, UPS and even Domino’s is investing in drone delivery services. [Online]. Available: <https://www.insiderintelligence.com/insights/drone-delivery-services/>
- [4] W. J. Yun, S. Jung, J. Kim, and J.-H. Kim, “Distributed deep reinforcement learning for autonomous aerial eVTOL mobility in drone taxi applications,” *ICT Express*, vol. 7, no. 1, pp. 1–4, 2021.
- [5] D. Erdos, A. Erdos, and S. E. Watkins, “An experimental UAV system for search and rescue challenge,” *IEEE Aerosp. Electron. Syst. Mag.*, vol. 28, no. 5, pp. 32–37, May 2013.
- [6] Y. Zeng, J. Lyu, and R. Zhang, “Cellular-connected UAV: Potential, challenges, and promising technologies,” *IEEE Wireless Commun.*, vol. 26, no. 1, pp. 120–127, Feb. 2019.
- [7] D. W. Matolak and R. Sun, “Unmanned aircraft systems: Air-ground channel characterization for future applications,” *IEEE Veh. Technol. Mag.*, vol. 10, no. 2, pp. 79–85, May 2015.
- [8] W. Khawaja, O. Ozdemir, F. Erden, I. Guvenc, and D. W. Matolak, “Ultra-wideband air-to-ground propagation channel characterization in an open area,” *IEEE Trans. Aerosp. Electron. Syst.*, vol. 56, no. 6, pp. 4533–4555, June 2020.
- [9] A. Al-Hourani and K. Gomez, “Modeling cellular-to-UAV path-loss for suburban environments,” *IEEE Wireless Commun. Lett.*, vol. 7, no. 1, pp. 82–85, Feb. 2018.
- [10] P. Sinha and I. Guvenc, “Impact of antenna pattern on TOA based 3D UAV localization using a terrestrial sensor network,” *IEEE Trans. Veh. Technol.*, vol. 71, no. 7, pp. 7703–7718, Jul. 2022.
- [11] V. Marojevic, I. Guvenc, R. Dutta, M. L. Sichitiu, and B. A. Floyd, “Advanced Wireless for Unmanned Aerial Systems: 5G Standardization, Research Challenges, and AERPAW Architecture,” *IEEE Veh. Technol. Mag.*, vol. 15, no. 2, pp. 22–30, 2020.
- [12] S. J. Maeng, O. Ozdemir, I. Guvenc, M. Sichitiu, R. Dutta, and M. Mushi, “AERIQ: SDR-Based LTE I/Q Measurement and Analysis Framework for Air-to-Ground Propagation Modeling,” in *Proc. IEEE Aerospace Conf.*, Big Sky, MT, USA, Mar. 2023.
- [13] W. C. Jakes and D. C. Cox, *Microwave mobile communications*. Wiley-IEEE press, 1994.
- [14] S. J. Maeng, O. Ozdemir, I. Guvenc, and M. Sichitiu, “3D antenna pattern measurement for AERPAW experiments,” *IEEE Dataport*, 2023. [Online]. Available: <https://dx.doi.org/10.21227/mma2-0t93>
- [15] Octane Wireless, “SA-1400-5900 Data Sheet.” [Online]. Available: <https://www.octanewireless.com/product/sa-1400-5900-tri-band-stub-antenna/>
- [16] S. J. Maeng, M. A. Deshmukh, I. Güvenç, A. Bhuyan, and H. Dai, “Interference analysis and mitigation for aerial IoT considering 3D antenna patterns,” *IEEE Trans. Veh. Technol.*, vol. 70, no. 1, pp. 490–503, Jan. 2021.
- [17] C. A. Balanis, *Antenna theory: analysis and design*. John wiley & sons, 2016.
- [18] J. P. Snyder, *Flattening the earth: two thousand years of map projections*. University of Chicago Press, 1997.
- [19] I. Guvenc, S. Gezici, and Z. Sahinoglu, “Fundamental limits and improved algorithms for linear least-squares wireless position estimation,” *Wirel. Commun. Mob. Comput.*, vol. 12, no. 12, pp. 1037–1052, Aug. 2012.
- [20] H. Kwon, S. J. Maeng, and I. Guvenc, “RF SSSL by an Autonomous UAV with Two-Ray Channel Model and Dipole Antenna Patterns,” in *Proc. IEEE Personal, Indoor, Mobile Radio Communications Workshops (PIMRC Workshops)*, Toronto, ON, Canada, Sep. 2023.
- [21] I. Guvenc and C.-C. Chong, “A survey on TOA based wireless localization and NLOS mitigation techniques,” *IEEE Communications Surveys & Tutorials*, vol. 11, no. 3, pp. 107–124, 2009.
- [22] P.-C. Chen, “A non-line-of-sight error mitigation algorithm in location estimation,” in *Proc. IEEE Wireless Commun. Netw. Conf.*, vol. 1, New Orleans, LA, USA, Sep. 1999, pp. 316–320.